Self-regulation of phenotypic noise synchronizes emergent organization and active transport in confluent microbial environments

Dhar, J.; Thai, A.N.P.; Ghoshal, A.; Giomi, L.; Sengupta, A.

nature physics

ARTICLES

https://doi.org/10.1038/s41567-022-01641-9

Check for updates

OPEN

Self-regulation of phenotypic noise synchronizes emergent organization and active transport in confluent microbial environments

Jayabrata Dhar[1], Anh L. P. Thai[1], Arkajyoti Ghoshal[1], Luca Giomi[2] and Anupam Sengupta[1]✉

The variation associated with different observable characteristics—phenotypes—at the cellular scale underpins homeostasis and the fitness of living systems. However, if and how these noisy phenotypic traits shape properties at the population level remains poorly understood. Here we report that phenotypic noise self-regulates with growth and coordinates collective structural organization, the kinetics of topological defects and the emergence of active transport around confluent colonies. We do this by cataloguing key phenotypic traits in bacteria growing under diverse conditions. Our results reveal a statistically precise critical time for the transition from a monolayer biofilm to a multilayer biofilm, despite the strong noise in the cell geometry and the colony area at the onset of the transition. This reveals a mitigation mechanism between the noise in the cell geometry and the growth rate that dictates the narrow critical time window. By uncovering how rectification of phenotypic noise homogenizes correlated collective properties across colonies, our work points at an emergent strategy that confluent systems employ to tune active transport, buffering inherent heterogeneities associated with natural cellular environment settings.

Microbial life, at the level of individual cells, is inherently noisy due to the intrinsic stochasticity of gene expressions[1–3], compounded by variations in the biotic and abiotic components in microbial habitats[4–6]. In bacteria, heterogeneity in phenotypic traits, including cell geometry, motility and surface association, enhance fitness and functionality[7–9], modulate chemotactic attributes[10,11], support homeostasis[12,13] and regulate bet-hedging strategies[14,15]. Whether the ramifications of related phenotypic noise, that is, cell-to-cell variability, on growing populations are suppressed or reinforced have been studied in single phenotypic contexts[16], yet, in nature, phenotypic traits can diversify concurrently[17,18]. It thus remains to be understood how variability across multiple phenotypes co-emerges and, crucially, if crosstalk therein could rectify noisy effects to trigger emergent collective properties, which are statistically deterministic in nature.

Recent experiments and modelling of growing bacterial colonies—a focal point in ecology, medicine and industry—have indicated the critical role of cell geometry and growth dynamics in shaping the properties of growing bacterial layers[19–25]. The emergence of structural order and low-dimensional topological attributes, including singularities (topological defects), are implicated in the morphogenesis of two-dimensional (2D) sessile colonies to 3D biofilms over longer timescales. Specifically, the mono-to-multilayer transition (MTMT)—a critical step in biofilm development—initiates due to a biomechanical interplay of geometry, order and topology[26,27], as has also been observed in motile surface-associated swarms[28,29]. The ability of bacteria to collectively exploit topological properties for optimal navigation strategies[30], localizing sporulation sites[31] and, potentially, for driving local nutrient fluxes[32,33] showcases emergent functionalities that bacteria can harness across a range of physiological timescales.

Despite recent mechanistic insights, the consequence of phenotypic noise on population-scale attributes, specifically in the context of emergent collective properties of microbial active matter, is yet to be understood. In this Article we bridge this conspicuous gap by combining single-cell time-lapse imaging, particle image velocimetry, numerical simulations and continuum modelling to quantify phenotypic noise associated with key traits, and analyse the role of noise in shaping two fundamental collective and correlated properties of confluent colonies: structural organization driving MTMT, in spatial correlation with the embedded topological defects, and the emergence of active local transport. We study the bacterial species *Escherichia coli* (strains C600-wt and NCM3722 delta-motA, hereafter Strain-1 and Strain-2, respectively) and *Serratia marcescens* (PCI 1107), growing under different conditions, allowing us to span a range of growth rates underpinning the expansion of confluent colonies (Methods section Bacterial cultures and bacteria-microparticle assays).

By tracking the expansion of confluent colonies through MTMT (Methods sections Time-lapse imaging and Image analysis and Fig. 1a,b), we quantify trait-specific phenotypic noise from the distributions of phenotypic traits at the critical time, t_c, the onset of the MTMT event (Supplementary sections A1 and A2). Our results reveal that trait-specific phenotypic noise autoregulates with growth (that is, colony age), such that with increasing intra-colony variability in time, the inter-colony variability reduces (Supplementary Fig. 1 and Supplementary section A3). At MTMT, phenotypic noise terms can differ over two orders of magnitude relative to each other: the cell aspect ratio (AR) and the critical colony area (A_c, colony area at t_c) are highly noisy, but the noise associated with t_c was the least (two orders lower), rendering MTMT a statistically precise event across all growth rates. We rationalize the emergence of the narrow t_c window—despite noisy phenotypic traits—with a continuum model of growing confluent colonies, uncovering a mitigation effect between the noise in the cell geometry and in the growth rate that tightens the distribution of t_c. Spatially, the out-of-plane extrusion occurs upon cell division, closer to the +1/2 than to the −1/2 defects present in the colony. We use a combination of particle tracking experiments and data-based theoretical computations over

[1]Physics of Living Matter, Department of Physics and Materials Science, University of Luxembourg, Luxembourg City, Luxembourg. [2]Instituut-Lorentz, Universiteit Leiden, Lieden, The Netherlands. ✉e-mail: anupam.sengupta@uni.lu

multiple layers to demonstrate that the structural dynamics in confluent colonies drive active transport in the micro-environment in a time-synchronous manner. By spanning diverse growth conditions and species, our work captures how autoregulation of phenotypic noise enables correlated collective phenomena—in structure, defect kinetics and active hydrodynamics—thereby establishing a general mechanistic framework to understand the emergence of statistically precise collective events within active systems comprising individuals that are intrinsically noisy or susceptible to systemic noise.

Critical time is deterministic despite high phenotypic noise. Cellular phenotypic traits, including length at birth (ℓ_b) and AR ($=\ell/w$, where ℓ and w are the bacterial length and width, respectively; Fig. 1c), show high variance at MTMT across all temperatures, following log-normal distributions (Supplementary sections A1 and A2 and Supplementary Figs. 3a,e, 4 and 5), in agreement with previous reports[34,35]. The log-normal nature of the ℓ_b and AR, which we confirm theoretically (equation (10a)), is observed frequently in natural systems and stems from the underlying independent random variables[34–37]. This confirms that the distribution of AR is ultimately determined by that of ℓ_b, provided the variability in growth rate remains low, as reported previously[38].

Despite the high variability in cell- and colony-scale descriptors at MTMT (Supplementary sections A1 and A2 and Supplementary Fig. 3), t_c is statistically precise, suggesting noise mitigation mechanisms across the phenotypic variabilities. Although A_c, both measured and predicted, is randomly distributed, with an overall high standard deviation (s.d.) across the growth temperatures (Fig. 1d), the mean and variation of t_c show an inverse relation with temperature (Fig. 1e). In contrast, the log-normal distribution of AR at MTMT suggests a high phenotypic noise across temperatures (Fig. 1f and Supplementary Fig. 3a), species and nutrient conditions (Supplementary Table 2 and Supplementary section B1). We discern the emergent crosstalk between phenotypic noise using a simple continuum model of an expanding colony, following ref. [26] (Methods section Hydrodynamic model and Supplementary Fig. 7), wherein MTMT occurs when cells experience longitudinal forces larger than

$$f_c \approx d_0 k_a \ell, \tag{1}$$

where d_0 is the cell diameter and $k_a\ell$, with k_a a constant and ℓ the cell length, is the total stiffness of the adhesion complex anchoring a cell to the substrate. As a consequence, newly divided cells are more likely to be extruded once the pressure in their surroundings exceeds the threshold $P_c = f_c/A_{cap}$, where $A_{cap} = \pi d_0^2/2$ is the area of the cells' spherical cap. The pressure field $P = P(r,t)$, with r the distance from the centre and t time, varies across the colony proportionally to the local packing fraction $\phi = \phi(r,t)$, that is, $P = P_0(\phi - 1)$, where P_0 is a constant independent of the growth rate[20]. Specifically, at the colony's centre (the probable site for the MTMT)

$$\phi(0,\ t) \approx \frac{A(t)}{A_0}, \tag{2}$$

where $A(t) = A_0 \exp k_d t$, with $k_d = \tau_d^{-1}\log 2$ and τ_d the area doubling time, is the colony's area (the approximation holds for long times; Methods section Hydrodynamic model). Thus, taking $P(0,\ t) = P_c$ and solving for the area gives

$$A_c = A_0(\ell/\ell_a + 1), \tag{3a}$$

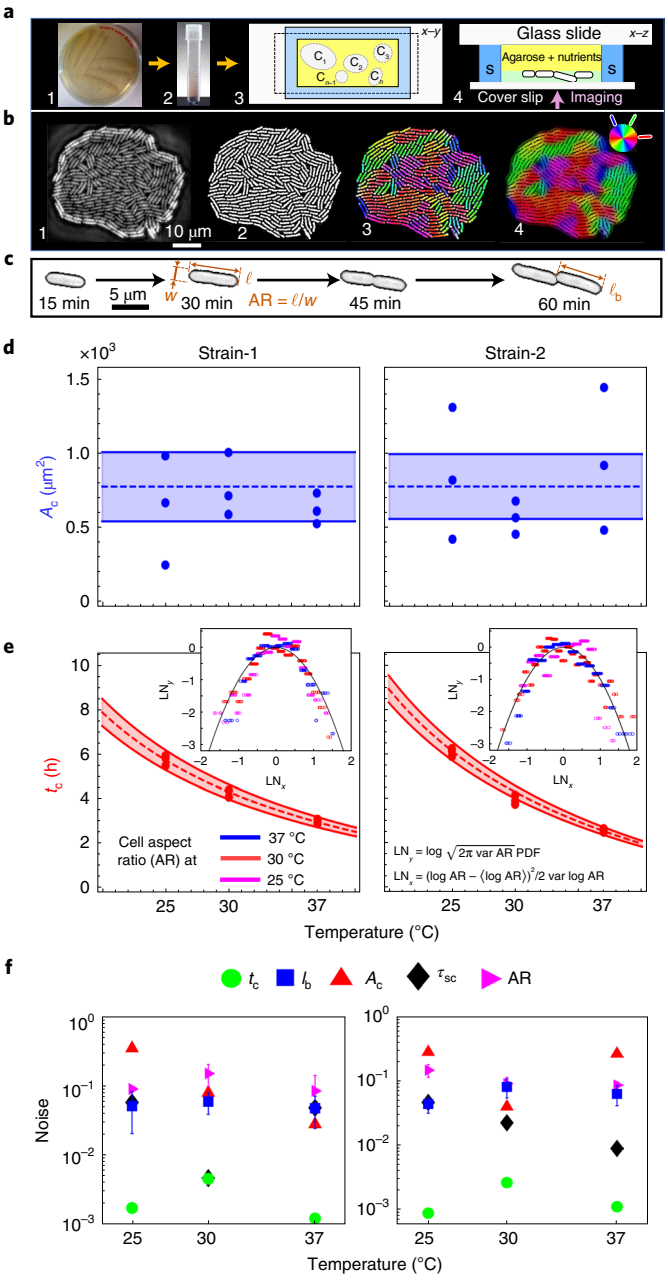

Fig. 1 | From noisy phenotypes to a statistically precise mono-to-multilayer transition event. a, Cells streaked on nutrient-rich agar plate (1) are transferred in the liquid medium (2), then seeded within the microfluidic chamber, here C_i denotes individual colonies (3), for phase-contrast time-lapse imaging (4) in the swimming pool (S). **b**, Raw images of growing colonies (1) are binarized to extract phenotypic traits (2) and colour-coded to visualize local cell orientation (3,4). **c**, Single-cell geometric traits: AR and ℓ_b. **d**,**e**, A_c is independent of growth temperature (**d**), as revealed both in our theory and experiments, whereas t_c is temperature-dependent (**e**). Blue and red points indicate distinct biological replicates (including multiple technical replicates) for A_c and t_c experimental data. A_c has large variance across all T, whereas t_c has low variance, which minimizes further with the growth temperature. Dashed lines and shaded regions indicate the mean and s.d. predicted using equations (5a) and (6a). Insets: the cell aspect AR ratio follows a log-normal distribution regardless of T, fitted by the LN_y versus LN_x curve (Supplementary Fig. 3a). **f**, Trait-specific phenotypic noise, quantified as the normalized variance, $F = \mathrm{var}(\cdots)/\langle\cdots\rangle^2$, across T: ℓ_b (blue squares), A_c (red triangles), cell length doubling time τ_{sc} (black diamonds), AR (magenta triangles) and t_c (green circles). Despite the high phenotypic noise at individual scales (ℓ_b, AR and τ_{sc}), t_c is statistically precise (corresponding noise is orders of magnitude lower across all T). The error bar denotes the standard deviation of F across colonies.

$$t_c = k_d^{-1}\log(\ell/\ell_a + 1), \tag{3b}$$

where $\ell_a = P_0 A_{cap}/(k_a d_0)$ is a constant length scale, expressing the typical extension of the adhesion molecules when stretched by force $P_0 A_{cap}$.

Equations (3a) and (3b) imply that the statistics of A_c and t_c are entirely determined by the probability distribution of the cellular length ℓ, which, in turn, is log-normal as shown in Fig. 1f. Thus, normalizing ℓ by ℓ_a and taking

$$\mathrm{PDF}(\ell/\ell_a) = \frac{1}{\sqrt{2\pi\sigma^2}\,\ell/\ell_a}\exp\left[-\frac{(\log\ell/\ell_a - \mu)^2}{2\sigma^2}\right], \tag{4}$$

with $\mu = \langle\log\ell/\ell_a\rangle$ and $\sigma^2 = \mathrm{var}(\log\ell/\ell_a)$, yields the approximation for mean value and variance of A_c

$$\langle A_c\rangle = A_0(\langle\ell/\ell_a\rangle + 1) \tag{5a}$$

$$\mathrm{var}\,A_c = A_0^2\mathrm{var}(\ell/\ell_a), \tag{5b}$$

and time

$$\langle t_c\rangle = k_d^{-1}\log(\langle\ell/\ell_a\rangle + 1), \tag{6a}$$

$$\mathrm{var}\,t_c = \left(\frac{k_d^{-1}}{\langle\ell/\ell_a\rangle + 1}\right)^2\mathrm{var}(\ell/\ell_a), \tag{6b}$$

where we have expanded t_c at the linear order about $\langle\ell/\ell_a\rangle$ to obtain equations (6a) and (6b). Then, using equation (4) allows us to explicitly compute the mean and variance of ℓ/ℓ_a in the form

$$\langle\ell/\ell_a\rangle = e^{\mu+\frac{1}{2}\sigma^2}, \tag{7a}$$

$$\mathrm{var}\,\ell/\ell_a = e^{2\mu+\sigma^2}\left(e^{\sigma^2} - 1\right). \tag{7b}$$

Finally, because the cellular length grows exponentially in time until reaching twice the length ℓ_b:

$$\ell(t) = 2^{t/\tau_d}\ell_b. \tag{8}$$

μ and σ^2 are, in principle, determined by the statistics of ℓ_b and τ_d, and, for sufficiently long times, the distribution of the doubling time is unimportant, because the mean and variance of the length solely depend on ℓ_b statistics. Specifically, normalizing both sides of equation (8) by ℓ_a and taking the logarithm gives

$$\log\ell/\ell_a = \log\ell_b/\ell_a + (t/\tau_d)\log 2. \tag{9}$$

Now, for $t \gg \tau_d$, the colony comprises a large number of cells, whose age is sufficiently diversified, their lengths thereby spanning the entire range $\ell_b \le \ell \le 2\ell_b$, and the time t in equations (8) and (9) can be treated as a uniformly distributed random variable in the range $0 \le t \le \tau_d$. Consequently, t/τ_d is a uniformly distributed random variable in the unit interval, from which $\langle t/\tau_d\rangle = 1/2$ and $\mathrm{var}(t/\tau_d) = 1/12$. Hence

$$\mu = \langle\log\ell_b/\ell_a\rangle + \frac{1}{2}\log 2, \tag{10a}$$

$$\sigma^2 = \mathrm{var}\ell_b/\ell_a + \frac{1}{12}(\log 2)^2. \tag{10b}$$

In summary, our theoretical analysis reveals that the statistics of A_c and t_c are ultimately determined by the distribution of ℓ_b, which, in turn, is log-normal, consistent with previous reports[34,35]. Given that temperature mainly affects the cell growth rate, while leaving the statistics of the length at birth essentially unaltered (Supplementary Fig. 3a–e), we infer that, regardless of the strains, both $\langle A_c\rangle$ and $\sqrt{\mathrm{var}A_c}$ are independent of temperature, whereas $\langle t_c\rangle$ and $\sqrt{\mathrm{var}t_c}$ vary inversely with T, because $k_d \sim T$ (Supplementary Fig. 3d). By comparing the measured and predicted mean A_c and t_c (Fig. 1d,e), we show that the blue (red) shaded regions are delimited by the respective standard deviations, obtained from the square root of equations (5b) and (6b). Consistent with our predictions, $\langle A_c\rangle$ is temperature-independent, whereas $\langle t_c\rangle$ varies inversely with T.

The phenotypic noise, quantified as the normalized variance of the measured parameters, $F = \mathrm{var}(\cdots)/\langle\cdots\rangle^2$ (Fig. 1f), spans nearly two orders of magnitude for a growth temperature. The noise is maximum for A_c (red triangles, $F \approx 0.1$), whereas t_c (green circles) shows the least noise, $F \approx 0.001$. The noise associated with other traits fall within these values ($0.001 < F < 0.1$). Our experimental data, supported by theory, suggest that the noise associated with cell elongation rate (k_{sc}) and the cell length distribution (ℓ/ℓ_a) crosstalk to yield a mitigation effect, resulting in $\ell/\ell_a \sim f(k_{sc})$ (see Methods section Hydrodynamic model for the correlation between k_d and k_{sc}).The noise in A_c and t_c, differing by two orders of magnitude, is reasonably validated in our theoretical model (equation (18) and Methods section Noise and activity underpin emergent trade-off). The dependence of ℓ on k_{sc} reduces the variance in t_c as the growth rate increases, ultimately leading to a noise-mitigating effect that regulates the precise timing of the MTMT events.

Bacteria extrude out of plane near +1/2 topological defects. Topological defects nucleate at the intersection of nematic microdomains in expanding bacterial colonies due to the anisotropic cell shape, AR > 1 (refs. [20,21,26,27,31]). A snapshot of defects at the MTMT is shown in Fig. 2a (right column) and Supplementary Fig. 8. The out-of-plane extrusion of the bacterial monolayer is triggered by freshly divided cells within the P-zone (Supplementary Fig. 7), a region in confluent colonies where the growth-induced in-plane active stresses and the surface-induced vertical restoring forces favour extrusion[26]. Figure 2a (left column) shows that multiple extrusion sites, lying in the vicinity of the topological defects, can emerge in an expanding colony (indicated by yellow arrow heads). Although all extrusion events were localized close to topological defects, not every defect triggers extrusion. MTMT occurs close to defects only when the defects lie within the P-zone (Fig. 2a and Supplementary Fig. 7) at the instance of cell division, shown in Fig. 2b. The probability of the out-of-plane extrusion decreases as one moves away from the colony centre, because the critical stress criterion is no longer fulfilled. So, despite cells dividing outside the P-zone, they do not trigger extrusion. Spatially, the extrusion sites are weakly correlated with the nature of the topological defects: the probability of extrusion is slightly higher next to the +1/2 topological defects (Fig. 2c,d and Supplementary Fig. 9a,b). Overall, the trend is comparable with other living systems[39], but in confluent bacterial colonies, the probabilities are not markedly different.

As the maximum AR varies with growth stage and conditions (Supplementary Figs. 1, 3a and 6), the number of potential defect sites—at the intersection of the domains—depends on the characteristic size of the nematic microdomains within a colony[20]. At MTMT, the number of defects, N_d, and the defect density ($C_d = N_d/A$), did not show a dependence on the growth rate, staying nearly uniform (Fig. 2e,f and Supplementary Fig. 8). For Strain-1, N_d was in the range $6 < N_d < 8$, and for Strain-2 it was in the range $8 < N_d < 11$. At 37 °C, 30 °C and 25 °C, the number of defects for Strain-1 (Strain-2) varied, respectively, as (mean ± s.d.) 6 ± 1 (8 ± 1), 7 ± 2 (11 ± 1) and 5 ± 2 (10 ± 3). In contrast, the rate of generation of defects at MTMT,

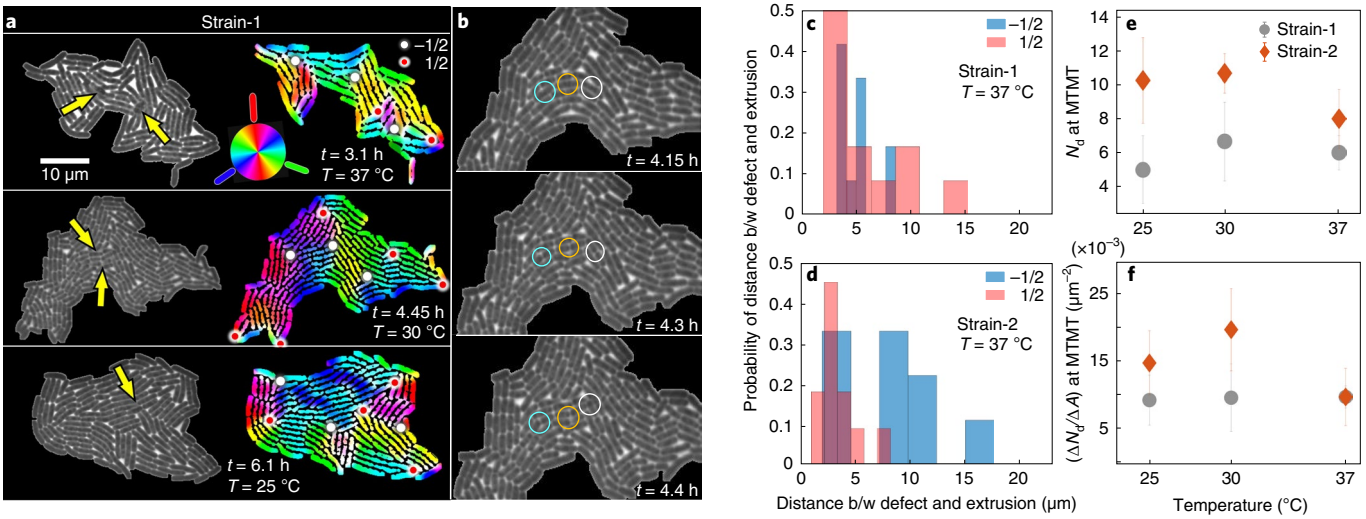

Fig. 2 | Kinetics and distribution of topological defects during MTMT. a, Out-of-plane extrusion can occur at multiple sites, as indicated by yellow arrows (left column). Distribution of topological defects at the onset of MTMT. False colours capture the orientation of nematic microdomains (right column). **b**, Image sequence of cell division leading to MTMT at $T = 30$ °C, capturing the bacterial monolayer (top), the instance of cell division (middle) and the onset of MTMT (bottom). MTMT closely follows the cell division event because shorter cells are easily extruded out of plane. Multiple extrusion events can occur simultaneously (cyan, yellow and white circles), if they are localized within the central P-zone. **c**,**d**, The probability of the location of an extrusion event ($x = 0$) in the vicinity of +1/2 and −1/2 topological defects for Strain-1 (**c**) and Strain-2 (**d**). The probability of extrusion is marginally higher next to a +1/2 defect than to a −1/2 defect. **e**,**f**, The number of topological defects in the confluent colony at MTMT (**e**) and the corresponding defect density normalized by the colony area (**f**). For a given strain, the number of topological defects at MTMT remains the same across all temperatures, but the rate of defect generation at MTMT increases with temperature, that is, with the bacterial growth rate.

$\Delta N_d/\Delta t$, increases with temperature. Because higher temperatures accelerate the cascade of biophysical events, $\Delta N_d/\Delta t$ shows a direct dependence on both the population growth rate, k_n, and the cell elongation rate, k_{sc} (Supplementary Figs. 3 and 9c). Taken together, our results demonstrate that, at MTMT, the kinetics of topological defects is regulated weakly by the temperature-dependent activity and more profoundly by the cell AR. This, thus allows for considering AR as a fundamental determinant of the topological manifestations in growing confluent colonies.

Emergent organization cascades to 3D active local transport. The log-normal statistics, alongside anisotropic morphology, underpin the statistically precise critical time of MTMT (t_c), establish the topological kinetics and regulate time-synchronous active transport properties. The flow vorticity and divergence distributions (Fig. 3a,b), extracted from time-lapse data (Methods and Supplementary Figs. 11, 12 and 13), present the growth-mediated hydrodynamics of confluent colonies. Positive and negative vortices, distributed equally (Fig. 3b, left and middle panel insets) alongside flow divergence, gain strength with increasing activity, thus reaching a maximum at 37 °C (Supplementary Fig. 12). The mean absolute vorticity (MAV, Fig. 3b), equivalent to the normalized enstrophy[40], measures the growth-induced kinetic energy input to the expanding colony. This, together with positive net mean divergence, suggests that, post-MTMT, confluent colonies can activate transport in their micro-environment. As growth temperature increases, the peaks of MAV and vorticity frequency become increasingly correlated with the MTMT event (Fig. 3b, right panel inset and Supplementary Fig. 3f), and vice versa, confirming a time-synchronous cascade from the structural transition to the emergent hydrodynamics in confluent bacterial colonies.

Sessile bacteria lack motility, so emergent hydrodynamics can be consequential for active transport in the colony micro-environment. Using numerical modelling, we characterized local transport around expanding colonies (Methods and Supplementary Figs. 14 and 15). Figure 3b (right) presents the enhanced transport, $(D/D_B)_{z=z_1}$, as the ratio of the effective and Brownian diffusion, simulated based on our experimental data, shown here for Strain-1 (Supplementary Fig. 12 presents the results for Strain-2). Despite lacking cellular motility, remarkably, expanding colonies enhance local transport, which increases with activity (here, T). For monolayers, the enhancement $(D/D_B)_{z=z_1}$ was approximately fourfold for 200-nm-diameter micro-cargo and tunable via temperature-dependent growth. Importantly, we captured a time-synchrony between the peak of $(D/D_B)_{z=z_1}$ relative to t_c (Fig. 3b, right, inset), suggesting temporal programmability of the local transport properties mediated by the structural changes.

At MTMT, the structural transition results in an out-of-plane vertical speed $W_{z=z_2}$ that we obtain from the PIV analysis of multilayer confluent colonies (Fig. 4a,b, orange). The expansion of the second layer contributes to the transport enhancement $(D/D_B)_{z=z_2}$, its magnitude set by the areal expansion rate of the second layer (Methods section Bacterial cultures and bacteria-microparticle assays and Supplementary Figs. 17 and 16). With active transport generated by each of the subsequent layers, the cumulative transport in the micro-environment becomes integrated as monolayers transform into multiple layers (Supplementary Fig. 17). The choice of viscosity (50 Pa s) in our in silico experiments represents a conservative estimate, as mucilaginous and exopolymeric substances associated with bacterial colonies can be as high as 10^3 Pa s (ref. [41]). Such viscous-dominated settings can amplify active transport nonlinearly, as demonstrated through the phase space of local viscosity and micro-cargo size (Supplementary Fig. 15; see Methods section Data-based transport simulations for details). For viscosity below 1 Pa s and for particles smaller than 100 nm in diameter, no effective enhancement was measured.

We visualized the ramifications of activity-driven enhanced transport using tracer experiments. The trajectories of tracers (mean diameter of 2 μm) suspended around confluent colonies reveal micro-cargo transport. Remarkably, despite the low local viscosity

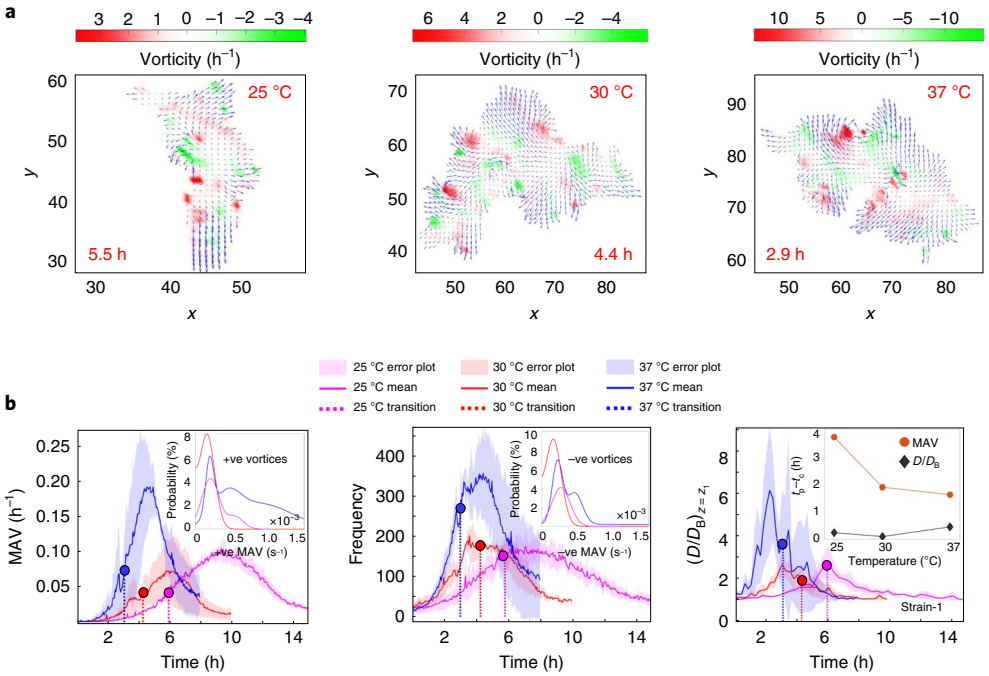

Fig. 3 | Structural organization during MTMT drives active micro-environmental transport synchronously. a, An interplay of growth- and surface-induced stresses drives emergent hydrodynamics in confluent colonies (shown here for Strain-1; corresponding Strain-2 data are presented in the Supplementary Information). Left to right: emergent vorticity fields at t_c strengthen as the temperature (and growth rate) increases from 25 °C to 30 °C and to 37 °C. Supplementary Video 1 and Supplementary Fig. 12 capture the evolution of the velocity fields and corresponding divergence fields. **b**, MAV (left) and the number of unique vortices (middle) at MTMT (indicated by dashed vertical lines) show a clear dependence on the growth temperature. Positive and negative vortices are distributed with equal probabilities (insets and Supplementary Fig. 13). Right: enhancement of transport above Brownian diffusion, computed from the experimental data, captures the emergence of active transport due to the expansion of the bacterial monolayer ($z = z_1$). The effective diffusion ratio, $(D/D_B)_{z=z_1}$, increases with the growth rate. Inset: the time difference between the peak of $(D/D_B)_{z=z_1}$ and MTMT, $t_p - t_c \approx 0$ h, confirming a strong temporal correlation (time-synchrony) between the peak of the active transport and MTMT across all temperatures.

(~0.25 Pa s), the expanding confluent colonies could substantially displace tracers and their self-organized clusters (Fig. 4c for $t = 0$ and 3.5 h and Supplementary Figs. 18–21). The enhanced transport de-clustered tracers over time, reducing the coordination number CN, the number of direct neighbours with which each particle is in contact (Fig. 4d, top inset). For the control case (without bacteria), the CN remained constant over a long time (Supplementary Video 2C). The rate of change of CN depends on the bacterial activity (and hence growth temperature; Supplementary Figs. 19 and 20). Finally, variation of the area of ellipses bounding the clusters (A_p) over time gives a measure of the strength of the active flows and their temperature-dependent modulation (Fig. 4d and Supplementary Fig. 19 and 20). Here we would like to highlight that Brownian diffusion of tracer clusters—orders of magnitude lower than single tracer particles[42]—fails to break apart isolated clusters (control case, Supplementary Video 2C). However, clusters in the colony micro-environment were successfully de-clustered. In view of the transport-driven de-clustering, our analytical model (developed for single particles) under-predicts the strength of the transport observed in our experiments, suggesting active transport regimes that are potentially stronger than what we have predicted. Experiments are underway to discern the nature of interactions between the passive clusters and confluent colonies.

From noise-mediated active processes to biological functions. By harnessing temperature as a tractable parameter for tuning biophysical activity, we could control the emergent structure and active transport in confluent bacterial colonies. We establish a generalized mechanistic link between biological activity and emergent properties in noisy systems that is applicable for different growth conditions and species. The data-based continuum modelling, combined with hydrodynamic simulations, quantifies how autoregulation of cellular phenotypic noise mitigates colony-scale variability, to ultimately drive structural transition, topological defect kinetics and active transport at the onset of biofilm formation. Time-synchrony, the specific temporal sequence of emergent structure and active flow phenomena, along with the activity-governed ability of colonies to tailor local transport attributes—despite noisy phenotypic traits—suggests potential physiological functions of such active phenomena, including molecular and material cargo transport at microscales. Expanding colonies exhibit strain- and activity-dependent phenotypic noise, yet, crucially, we discover that 2D to 3D morphological transitions are insulated from noise, rendering MTMT a statistically precise process in the life of a confluent colony. Downstream, MTMT triggers time-synchronized active hydrodynamic properties, ultimately driving enhanced transport in colony micro-environments. In natural settings, such time-synchronized active phenomena could enable the extruded cells forming the second layer (and beyond) to access resources, as these cells lose direct access to nutrients through contact with the nutrient-rich substrate. Interestingly, the high local viscosity characteristic of exopolymeric substance-rich bacterial colonies (10^3 Pa s; ref. [41]) promotes enhancement of active transport non-linearly, potentially enabling patchy-to-homogenized resource distribution (for example, molecular concentrations) at the onset of the extrusion events. Further afar, confluent colonies can harness active flows for shuttling sub-micrometre- to micrometre-sized microbial cargo (fungal spores and bacterial cells), liposomes and extracellular vesicles delivering genetic or biochemical cargo, hitchhiking bacteriophages and synthetic beads and capsules relevant

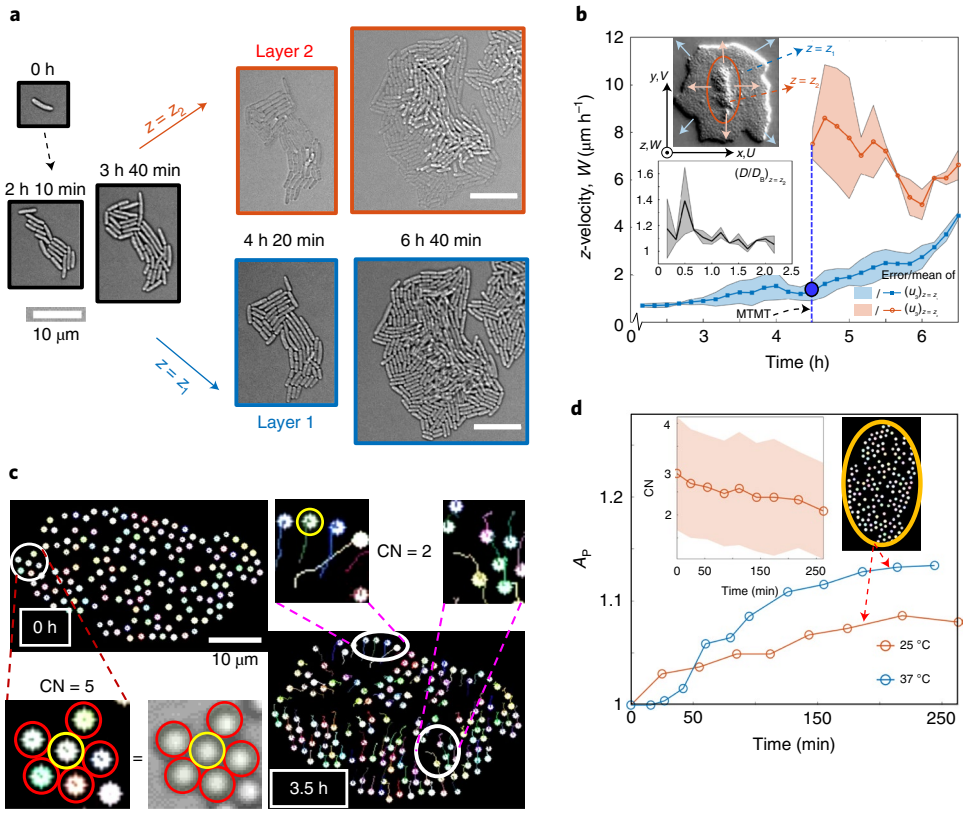

Fig. 4 | Enhanced local transport and its ramifications. a, Tracking colony growth in the first and second layers, captured by focusing each bacterial plane (Methods section Image analysis and Supplementary Fig. 16) to extract the layer-wise diffusion coefficients. **b**, The out-of-plane vertical speed $W_{z=z_{1,2}}$ obtained from the PIV analysis of confluent layers pre- and post-MTMT event reveals enhancement of vertical speed at the onset of MTMT, which persists as the second layer expands ($z=z_2$, top inset micrograph, shown for Strain-2 at 30 °C). With additional active transport generated by the expanding second layer (bottom inset shows $(D/D_B)_{z=z_2}$), the net transport will amplify as multiple layers form (Supplementary Fig. 17). **c**, Harnessing active flows in confluent colonies, demonstrated by de-clustering and transport of suspended tracers. The coordination number CN, the number of particles in contact (red) with the particle of interest (yellow) drops as the colony expands (**d**, inset), in contrast to the control case (no bacteria), where the clusters persist. **d**, The strength of de-clustering and transport, measured by the area of the bounding ellipse (A_p), increases with growth temperature. See Supplementary Section D, Supplementary Video 2 and Supplementary Figs. 19 and 20 for the de-clustering dynamics. Solid lines and shaded areas denote the mean and s.d., respectively.

for drug delivery (see discussion in Supplementary section A4). Confluent microbial active matter is a multifield topological system[43] in which the topology of structure, active hydrodynamics and microscale transport emerge sequentially with respect to the onset of the MTMT. The geometric and topological interplay ultimately translates into multifold enhancement of the transport in the colony vicinity, despite the cells being non-motile. The multifield topological facets uncovered here further our mechanistic understanding of diverse confluent systems[39,44–46], extending our classical view of active and emergent properties, specifically in the context of cell-scale phenotypic noises and their mitigating effects on population-scale variability, across geometric, topological and hydrodynamic properties. The biological significance of the time-synchronous nexus of structure–flow–transport is multi-pronged: strict timing of the extrusion events presents MTMT as a proxy to quorum-like sensing between the colonies, with potential ramifications of and in synchronous selection for resistant cells (for example, against antibiotics). Disrupting the well-defined MTMT timing could offer future alternatives to inhibit quorum-sensing, and thereby tailor bacterial resistance to antibiotics. Looking ahead, it will be critical to understand how inter-colony communications emerge under stressful environments, in the parameter space of intrinsic noise and structure–flow time-synchronicity. Finally, the noise-mediated spatio-temporal phenomena presented here could provide key missing insights into the biophysics of morphogenesis in systems with higher complexity, including polymicrobial consortia observed in human and plant microbiomes, and multicellular tissue systems relevant for embryonic and cancer development (Supplementary section A4).

Online content

Any methods, additional references, Nature Research reporting summaries, source data, extended data, supplementary information, acknowledgements, peer review information; details of author contributions and competing interests; and statements of data and code availability are available at https://doi.org/10.1038/s41567-022-01641-9.

Received: 23 May 2021; Accepted: 18 May 2022;
Published online: 4 July 2022

References

1. Thomas, P., Terradot, G., Danos, V. & Weiße, A. Y. Sources, propagation and consequences of stochasticity in cellular growth. *Nat. Commun.* **9**, 4528 (2018).
2. Schmiedel, J. M., Carey, L. B. & Lehner, B. Empirical mean-noise fitness landscapes reveal the fitness impact of gene expression noise. *Nat. Commun.* **10**, 3180 (2019).

3. Thomas, P. Intrinsic and extrinsic noise of gene expression in lineage trees. *Nat. Commun.* **9**, 474 (2019).
4. Hilfinger, A. & Paulsson, J. Separating intrinsic from extrinsic fluctuations in dynamic biological systems. *Proc. Natl Acad. Sci. USA* **108**, 12167–12172 (2011).
5. Lidstrom, M. E. & Konopka, M. C. The role of physiological heterogeneity in microbial population behavior. *Nat. Chem. Biol.* **6**, 705–712 (2010).
6. Korobkova, E., Emonet, T., Vilar, J. M. G., Shimizu, T. S. & Cluzel, P. From molecular noise to behavioural variability in a single bacterium. *Nature* **428**, 574–578 (2004).
7. Hashimoto, M. et al. Noise-driven growth rate gain in clonal cellular populations. *Proc. Natl Acad. Sci. USA* **113**, 3251–3256 (2016).
8. Cerulus, B., New, A. M., Pougach, K. & Verstrepen, K. J. Noise and epigenetic inheritance of single-cell division times influence population fitness. *Curr. Biol.* **26**, 1138–1147 (2016).
9. Patange, O. et al. *Escherichia coli* can survive stress by noisy growth modulation. *Nat. Commun.* **9**, 5333 (2018).
10. Waite, A. J., Frankel, N. W. & Emonet, T. Behavioral variability and phenotypic diversity in bacterial chemotaxis. *Annu. Rev. Biophys.* **47**, 595–616 (2018).
11. Emonet, T. & Cluzel, P. Relationship between cellular response and behavioral variability in bacterial chemotaxis. *Proc. Natl Acad. Sci. USA* **105**, 3304–3309 (2008).
12. Taheri-Araghi, S. et al. Cell-size control and homeostasis in bacteria. *Curr. Biol.* **25**, 385–391 (2015).
13. Schwabe, A., Dobrzyński, M., Rybakova, K., Verschure, P. & Bruggeman, F. in *Methods in Systems Biology* Vol. 500 (eds Jameson, D., Verma, M. & Westerhoff, H. V.) Ch. 28, 597–625 (Academic Press, 2011).
14. Acar, M., Mettetal, J. T. & van Oudenaarden, A. Stochastic switching as a survival strategy in fluctuating environments. *Nat. Genet.* **40**, 471–475 (2008).
15. Ackermann, M. A functional perspective on phenotypic heterogeneity in microorganisms. *Nat. Rev. Microbiol.* **13**, 497–508 (2015).
16. Koutsoumanis, K. P. & Lianou, A. Stochasticity in colonial growth dynamics of individual bacterial cells. *Appl. Environ. Microbiol.* **79**, 2294–2301 (2013).
17. Dougherty, K. et al. Multiple phenotypic changes associated with large-scale horizontal gene transfer. *PLoS ONE* **9**, e102170 (2014).
18. Thöming, J. G. et al. Parallel evolutionary paths to produce more than one *Pseudomonas aeruginosa* biofilm phenotype. *npj Biofilms Microbiomes* **6**, 2 (2020).
19. Grant, M. A. A., Wacław, B., Allen, R. J. & Cicuta, P. The role of mechanical forces in the planar-to-bulk transition in growing *Escherichia coli* microcolonies. *J. R. Soc. Interface* **11**, 20140400 (2014).
20. You, Z., Pearce, D. J. G., Sengupta, A. & Giomi, L. Geometry and mechanics of microdomains in growing bacterial colonies. *Phys. Rev. X* **8**, 031065 (2018).
21. Dell'Arciprete, D. et al. A growing bacterial colony in two dimensions as an active nematic. *Nat. Commun.* **9**, 4190 (2018).
22. Echten, D. v. H. t., Nordemann, G., Wehrens, M., Tans, S. & Idema, T. Defect dynamics in growing bacterial colonies. Preprint at https://arxiv.org/abs/2003.10509 (2020).
23. Warren, M. R. et al. Spatiotemporal establishment of dense bacterial colonies growing on hard agar. *eLife* **8**, e41093 (2019).
24. Beroz, F. et al. Verticalization of bacterial biofilms. *Nat. Phys.* **14**, 954–960 (2018).
25. Hartmann, R. et al. Emergence of three-dimensional order and structure in growing biofilms. *Nat. Phys.* **15**, 251–256 (2019).
26. You, Z., Pearce, D. J. G., Sengupta, A. & Giomi, L. Mono- to multilayer transition in growing bacterial colonies. *Phys. Rev. Lett.* **123**, 178001 (2019).
27. Sengupta, A. Microbial active matter: a topological framework. *Front. Phys.* **8**, 184 (2020).
28. Copenhagen, K., Alert, R., Wingreen, N. S. & Shaevitz, J. W. Topological defects promote layer formation in *Myxococcus xanthus* colonies. *Nat. Phys.* **17**, 211–215 (2021).
29. Patteson, A. E., Gopinath, A. & Arratia, P. E. The propagation of active-passive interfaces in bacterial swarms. *Nat. Commun.* **8**, 5373 (2018).
30. Meacock, O. J., Doostmohammadi, A., Foster, K. R., Yeomans, J. M. & Durham, W. M. Bacteria solve the problem of crowding by moving slowly. *Nat. Phys.* **17**, 205–210 (2021).
31. Yaman, Y. I., Demir, E., Vetter, R. & Kocabas, A. Emergence of active nematics in chaining bacterial biofilms. *Nat. Commun.* **10**, 2285 (2019).
32. Mathijssen, A. J. T. M., Guzmán-Lastra, F., Kaiser, A. & Löwen, H. Nutrient transport driven by microbial active carpets. *Phys. Rev. Lett.* **121**, 248101 (2018).
33. Guzmán-Lastra, F., Löwen, H. & Mathijssen, A. J. T. M. Active carpets drive non-equilibrium diffusion and enhanced molecular fluxes. *Nat. Commun.* **12**, 1906 (2021).
34. Campos, M. et al. A constant size extension drives bacterial cell size homeostasis. *Cell* **159**, 1433–1446 (2014).
35. Amir, A. Cell size regulation in bacteria. *Phys. Rev. Lett.* **112**, 208102 (2014).
36. Ottino-Loffler, B., Scott, J. G. & Strogatz, S. H. Evolutionary dynamics of incubation periods. *eLife* **6**, e30212 (2017).
37. Hosoda, K., Matsuura, T., Suzuki, H. & Yomo, T. Origin of lognormal-like distributions with a common width in a growth and division process. *Phys. Rev. E* **83**, 031118 (2011).
38. Wallden, M., Fange, D., Lundius, E. G., Baltekin, Ö. & Elf, J. The synchronization of replication and division cycles in individual *E. coli* cells. *Cell* **166**, 729–739 (2016).
39. Saw, T. B. et al. Topological defects in epithelia govern cell death and extrusion. *Nature* **544**, 212–216 (2017).
40. Lin, S.-Z., Zhang, W.-Y., Bi, D., Li, B. & Feng, X.-Q. Energetics of mesoscale cell turbulence in two-dimensional monolayers. *Commun. Phys* **4**, 21 (2021).
41. Gloag, E. S., Fabbri, S., Wozniak, D. J. & Stoodley, P. Biofilm mechanics: implications in infection and survival. *Biofilm* **2**, 100017 (2020).
42. Anthony, S. M., Kim, M. & Granick, S. Translation-rotation decoupling of colloidal clusters of various symmetries. *J. Chem. Phys.* **129**, 244701 (2008).
43. Giomi, L., Kos, Z., Ravnik, M. & Sengupta, A. Cross-talk between topological defects in different fields revealed by nematic microfluidics. *Proc. Natl Acad. Sci. USA* **114**, E5771–E5777 (2017).
44. Grobas, I., Polin, M. & Asally, M. Swarming bacteria undergo localized dynamic phase transition to form stress-induced biofilms. *eLife* **10**, 1325–1334 (2021).
45. Turiv, T. et al. Topology control of human fibroblast cells monolayer by liquid crystal elastomer. *Sci. Adv.* **6**, eaaz6485 (2020).
46. Guillamat, P., Blanch-Mercader, C., Kruse, K. & Roux, A. Integer topological defects organize stresses driving tissue morphogenesis. *Nat. Mater.* **21**, 588–597 (2022).

Methods

Bacterial cultures and bacteria-microparticle assays. *Bacterial cultures.* We used two non-motile strains of *E. coli* bacteria, namely C600-WT and NCM3722 (Strain-1 and Strain-2, respectively). We considered a minimum of three biological replicates for our bacterial experiments at each temperature and for each strain in this study. As a first step, the cells were streaked on standard agar plates replete with lysogeny broth (LB). The plated cells were grown for a day, after which isolated cell colonies were identified and scraped using a sterile microbiological loop. Depending on the downstream experimental requirements, the growth temperature in each step of cell culturing was set to one of the temperatures considered in this work (25 °C, 30 °C and 37 °C). The scraped cells were then transferred to liquid LB medium, and allowed to divide in a shaker for ~12 h. The culture was subsampled at regular intervals to track the cell growth over time, using the optical density (OD) measurement technique. After nearly 12 h of liquid culture growth, the cells were transferred into fresh LB medium at a 1:1,000 ratio of cells to fresh medium, then grown for ~2 h, before they were introduced onto the specially designed substrates (Fig. 1) for time-lapse imaging of the colony expansion at 25 °C, 30 °C and 37 °C. We used growth temperature, a key determinant of physiology, viability and pathogenicity of bacteria[47–50], to regulate the biophysical activity of the proliferating colonies. The effects of temperature on bacterial metabolism are well supported by mathematical models and data-backed empirical formulations[50], yet temperature-dependent tuning of the biophysical activity, at either individual or colony scales, has remained unexplored in bacterial active matter. The single-cell-to-colony dynamics was observed using time-lapse microscopy on a 2-mm-thick layer of agarose gel. The gel was uniformly mixed with LB medium, a nutrient-rich medium commonly used for growing bacteria under laboratory settings (Fig. 1a). This nutrient-rich layer was sandwiched between two glass slides, and a 2-mm-thick Gene Frame (spacer) was used to enclose the glass-agarose system. A time-lapse phase-contrast microscope was used to image the cell dynamics from below. The protocols for the experiments with an additional species (*S. marcescens* PCI1107) and nutrient-limited NCM3722 are presented in Supplementary section B1.

Bacteria-particle assay for quantification of transport properties. To culture the bacteria along with the microparticles we used 2-μm-sized polystyrene beads (initial concentration of 98% vol/vol; Sigma-Aldrich). We first diluted the particles in sterilized de-ionized (DI) water (50 μl of the 2-μm particle solution in 1 ml of DI water). The mixture was vortexed and treated in a sonication bath for 2 min, then centrifuged (at 600 r.p.m.) for another 2 min. The agglomerated beads were separated and resuspended in DI water and the steps repeated, before introducing the suspension into 1 ml of LB medium. The mixture was sonicated again and then centrifuged for 2 min each, sequentially. The process was repeated three times to ensure the beads were finally suspended in 1 ml of LB medium, to reach a low final concentration of ~10^3 particles per ml. Finally, the 1 ml of LB medium + beads mixture was mixed with 5 ml of pure LB medium and sonicated for 2 min to hinder flocculation or particle sedimentation. The bacterial strains were cultured in 6 ml of LB + particle medium for each temperature used in the study. For propagation of the bacterial culture at each temperature in the LB + beads medium, we followed the same method as in the previous section. After an interval of 2 h, we observed the growth of the bacterial strain under the microscope to ascertain its fitness in the medium with beads. Our observations indicated that its fitness remained unchanged in the presence of beads. Bio-compatibility was tested by allowing the bacterial cells to grow in this dilute medium over multiple generations. We compared the growth rate and the geometry of individual cells (microscopy) across all temperatures, and compared them against the control data (cells grown without the microparticles). No difference could be statistically measured between the two sample sets, statistically ruling out cytotoxic effects due to the dilute particle suspension. After fabrication of the agarose substrate (described earlier, Fig. 1), growth of the colonies and concomitant particle transport were visualized at ×60 and ×40 magnifications, while maintaining the sample at a particular temperature (Time-lapse imaging). For visualization, we selected six colonies for each temperature and noted the x–y coordinates of their initial positions. After an interval of 30 min, the change in the positions of the beads was captured (an example is shown in Supplementary Fig. 21). From the captured images, the microparticles were identified and their centroids extracted using image analysis tools. The evolution of the position of the centroid of the beads was extracted using the Mosaic track package in ImageJ. The trajectories of the beads for all the captured colonies at each temperature provided us with the effective diffusion coefficient from the mean-squared displacement analysis. The evolution of the particle centroids was also used to quantify the coordination number, the bounding elliptical area of particle locations and the circularity of the bounding ellipse (see Supplementary Fig. 21 for details). For measurement of the coordination number, two particles were considered to be in contact when the centre-to-centre distance was less than the sum of the particle radii, with a tolerance of 10% of the particle radius.

Time-lapse imaging. For experimentation at each particular temperature, we cultured the cells overnight in LB medium and maintained the culture in a temperature-controlled shaker. For the present study, we maintained the cultures in 25 °C, 30 °C and 37 °C. A dilute concentration was extracted from the culture and placed on an agarose plate on which a single bacterium was spotted. The subsequent growth of this single bacterium into colonies was imaged while maintaining a temperature corresponding to the growth of the culture within the microscope environment. Such a single bacterium acts as the nucleating site for the growth of monoclonal colonies. For each strain and temperature we performed three sets of experiments. The statistics of our analysis were measured over all replicates. For the analysis of MTMT, we visualized more colonies in some cases to ascertain its lower variance. We observed a variability in morphological parameters such as length at birth and length at transition within colonies, even under similar conditions potentially attributable to phenotypic heterogeneity.

The colony growth in two dimensions and subsequent penetration to the third dimension was visualized using time-lapse phase-contrast microscopy. Images were acquired using a Hamamatsu ORCA-Flash camera (1 μm = 10.55 pixels) coupled to an inverted microscope (Olympus CellSense LS-IXplore) with a ×60 oil objective. Overall, this gave a resolution of 0.11 μm. The microscope stage was enclosed within a thermally insulated temperature-controlled incubator (Pecon), which could be regulated precisely to set the temperature, and we monitored the temperature at the sample with a resolution of 0.1 °C. Each experiment typically lasted between 15 h and 18 h, allowing us to capture the mono- to bilayer transitions (Supplementary Fig. 5) and further transitions from bi- to tri- and quadri-layers. Before initiation of capturing the images, we identified and recorded multiple locations on the agarose surface where a single bacterium was present. The microscope was automated to scan these pre-recorded coordinates and capture the images of the gradually increasing colonies at 3-min intervals while maintaining the focus across all the colonies captured. The images captured and saved over hours gave us the necessary data to analyse the MTMT, dynamics and transport within the bacterial colonies. We extracted the dimensions (width and length), position (centroid) and orientation of each bacteria from the phase-contrast images using a combination of the open-source packages of Ilastik[51] and ImageJ as well as MATLAB (MathWorks), as detailed in the next section. Upon extraction of the cell morphological properties, we were able to generate the orientation maps of the colony (Fig. 1b).

Image analysis. *Image segmentation, cell geometry analysis and cell counting.* The counting process consisted of cell segmentation followed by counting the number of individual entities. Cell segmentation was performed using a combination of Ilastik–MATLAB coding that helped to extract the bacterial length and orientation in the colony for each time frame of the bacterial colony growth. The process was continued until the colony encountered MTMT, because after this the image contrast and focus became too limited for subsequent segmentation to be carried out (PIV analysis, described in the following, was still feasible). Initially, pre-processing of the raw images was performed by a combination of background filling and weighted bottom-hat and top-hat filter application Supplementary Fig. S5. On the pre-processed image, Ilastik was trained for bacterial segmentation. The training process involved iteration until a reasonably satisfactory extraction was obtained. A labelled image was extracted from the segmentation process and identified in MATLAB. A bacillus-shaped water-shedding technique was performed to separate out joint bacterial cells. Finally, these individual entities (segmented cells) were coloured (Supplementary Fig. 4f) or outlined (Supplementary Fig. 6) for counting and analysis. The orientation of the individual bacteria led to an effective director profile of the microdomains emerging with the expanding colony (as shown in Fig. 1b). Details of the orientational analysis for microdomain detection are presented in ref. [20]. Once the microdomains were tracked, the topological defects were identified as the intersection of three or more microdomains, and further verified visually for all colony data. Depending on the rotational nature of the change in the microdomain orientations at the intersection (clockwise or counterclockwise, as for the polarization optics of topological defects in ordered materials), the defect sign was assigned as (+)ve or (−)ve.

Colony extraction and PIV analysis. Image processing was carried out using the MATLAB Image Processing module. In the following we describe the image-processing steps we used to extract the bacterial colony (in sequence): adaptive thresholding, image dilating and filling, then image labelling. The label that coincides with a given centre, which is any point on the first bacterial cell, was then extracted and dilated, again followed by image filling, then finally an image erosion was applied. A Boolean intersection carried out between the image from the last step and the original (raw) image satisfactorily extracted the outline of the colony at each time frame. The colony outline gave an effective colony area that changed with time and was tracked for each experiment.

PIV analysis was performed on the final extracted colony images (frames that not only preclude background noise in the flow due to colony growth and light interference, but also help focus on a single colony in cases where multiple colony growths were captured in a single frame). For the PIV analysis, the Contrast-Limited Adaptive Histogram Equalization (CLAHE) filter was initially applied to each image for better contrast. The fast Fourier transform-based cross-correlation algorithm was found to be optimal with a three-pass interrogation area. Specifically, the desired outputs from the PIV analysis are the two velocity components (U, V) and the vorticity field at each time frame, which is generated

within the bacterial colony due to its spread. To capture the out-of-plane velocity, multiple layers were captured by focusing on each bacterial plane. The individual layers were then extracted and analysed using PIV, allowing us to extract the U, V velocity field for each plane (Supplementary Fig. 16). Applying a no-slip boundary condition and continuity equation $\nabla \cdot \mathbf{v}$, we obtained the out-of-plane velocity field W. Knowing the velocity of the first layer and using the above constraints, the velocity of the second layer (after MTMT), was computed, as presented in Fig. 4b. The U, V velocity field was used to compute the local diffusion coefficient for each layer (Fig. 4b). The PIV analysis with the processed images was carried out with PIVlab—the particle image velocimetry (PIV) toolbox of MATLAB[52].

Hydrodynamic model. Next we provide a derivation of equation (2). The late temporal dynamics of growing colonies can be conveniently described upon modelling the colony as a 2D continuum, whose total mass $M=\int \mathrm{d}^2 r\rho$ ($\rho=\rho(\mathbf{r},t)$ is the density) grows exponentially in time and whose momentum density $\rho\mathbf{v}$ ($\mathbf{v}=\mathbf{v}(\mathbf{r},t)$ is the velocity) evolves under the combined effect of pressure gradients and drag. The corresponding hydrodynamic equations are given by

$$\partial_t \phi + \nabla \cdot (\phi \mathbf{v}) = k_\mathrm{d}\phi, \tag{11a}$$

$$\rho_\mathrm{cell}[\partial_t(\phi\mathbf{v}) + \nabla \cdot (\phi\mathbf{v}\mathbf{v})] = -\nabla P - \zeta\phi\mathbf{v}, \tag{11b}$$

where $\phi=\rho/\rho_\mathrm{cell}$ (ρ_cell is the average density of individual cells) is the local packing fraction, $k_\mathrm{d} = \tau_\mathrm{d}^{-1}\log 2$ (τ_d is the area doubling time), P is the pressure and ζ is a kinetic drag coefficient. On neglecting inertial effects, equation (11b) can be readily solved to give a Darcy-like expression for the velocity field, namely

$$\phi\mathbf{v} = -\frac{1}{\zeta}\nabla P. \tag{12}$$

Then, using the equation of state introduced in section Critical time is deterministic despite high phenotypic noise, that is $P=P_0(\phi-1)$, taking the divergence of equation (12) and replacing the resulting expression in equation (11a), yields a single partial differential equation for the packing fraction ϕ, that is

$$\partial_t \phi = D\nabla^2\phi + k_\mathrm{d}\phi, \tag{13}$$

where $D=P_0/\zeta$ is an effective diffusion coefficient. Equation (13) can be readily solved with initial conditions $\phi(\mathbf{r},0)=A_0\delta(\mathbf{r})$, where A_0 is the initial area of the colony. This gives

$$\phi(r,\ t) = \frac{A(t)}{4\pi D t}\mathrm{e}^{-\frac{r^2}{4Dt}}, \tag{14}$$

where

$$A(t) = \int \mathrm{d}^2 r\phi(\mathbf{r},\ t) = A_0\mathrm{e}^{k_\mathrm{d}t}, \tag{15}$$

is the area of the colony at time t. Now, at the centre of the colony one can approximate

$$\phi(0,\ t) = \exp\left(k_\mathrm{d}t - \log\frac{4\pi D t}{A_0}\right) \overset{k_\mathrm{d}t\gg 1}{\rightarrow} \mathrm{e}^{k_\mathrm{d}t}, \tag{16}$$

as long as

$$k_\mathrm{d} < \frac{4\pi D}{A_0}. \tag{17}$$

Finally, dividing and multiplying the right-hand side of equation (16) by A_0 and using equation (15) yields equation (2). Note that areal diffusion D and initial area A_0 have orders of magnitudes of $10^{-13}\,\mathrm{m^2\,s^{-1}}$ and $10^{-11}\,\mathrm{m^2}$. This makes the right-hand side of the ratio in the above equation in the range of $0.1\,\mathrm{s^{-1}}$ to $0.01\,\mathrm{s^{-1}}$. With doubling time being on the order of minutes, the corresponding value of k_d becomes $10^{-3}\,\mathrm{s^{-1}}$ or less, thereby bringing about experimental agreement with the above relation. We note that the relation $\tau_\mathrm{d}\sim\tau_\mathrm{sc}$ holds strongly for colonies with nearly perfect packing, that is, $NA_\mathrm{sc}=A$ (where A_sc is the area of a single cell), and constant bacterium width, as observed in the majority of our experiments (Supplementary Fig. 3[20]). Note that $k_\mathrm{sc}=\tau_\mathrm{sc}^{-1}\log 2$.

Noise and activity underpin emergent trade-off. To obtain the value F as a function of temperature (that is, biophysical activity) and noting that $F(x)=\mathrm{var}(x)/\langle x\rangle^2$, we recast equation (6a) as

$$F(t_\mathrm{c}) = \frac{F(\ell/\ell_\mathrm{a})}{k_\mathrm{d}^2(\frac{1}{\langle\ell/\ell_\mathrm{a}\rangle}+1)^2\langle t_\mathrm{c}\rangle^2} = \frac{F(A_\mathrm{c})}{k_\mathrm{d}^2\langle t_\mathrm{c}\rangle^2}. \tag{18}$$

A simplification of the above equation can be obtained by using equations (5a), (5b) and (6a), (6b). We can relate the magnitude of noise associated with the critical area and the time with that of the noise associated with the cell length, which in turn originates from the intrinsic randomness of the cell division process. Dividing equation (5a) by equation (5a) and using the fact that $\ell\gg\ell_\mathrm{a}$, one readily finds

$$F(A_\mathrm{c}) = \frac{\mathrm{var}\ell/\ell_\mathrm{a}}{(\langle\ell/\ell_\mathrm{a}\rangle+1)^2} \approx F(\ell), \tag{19}$$

$$F(t_\mathrm{c}) = \frac{\mathrm{var}\ell/\ell_\mathrm{a}}{(k_\mathrm{d}\langle t_\mathrm{c}\rangle)^2(\langle\ell/\ell_\mathrm{a}\rangle+1)^2} \approx \frac{F(\ell)}{(k_\mathrm{d}\langle t_\mathrm{c}\rangle)^2}. \tag{20}$$

Thus, although the critical area is affected by the same amount of noise as the cell length, from which noise originates, the critical time is substantially less noisy. This is by virtue of the fact that $\langle t_\mathrm{c}\rangle\gg\tau_\mathrm{d}$ and thus $k_\mathrm{d}\langle t_\mathrm{c}\rangle\gg 1$ and $F(t_\mathrm{c})\ll F(\ell)$.

Data-based transport simulations. To obtain a data-based effective diffusion coefficient from the colony-mediated hydrodynamics, we used the particle tracing approach, in which a certain number of particles are placed randomly in the flow field induced by the expanding bacterial colony. The positions of the particles are then tracked over time. Here the evolution of the particle position is achieved by simplifying the generalized Langevin equations. The force balance using 2D generalized Langevin equation formulations for massless particles with a background flow field reads $\zeta\frac{\mathrm{d}\mathbf{x}}{\mathrm{d}t} = \zeta\mathbf{v} + \zeta\sqrt{4D}\mathbf{W}(t)$, where $\mathbf{v}$ is the velocity field (induced due to the bacterial growth), $\mathbf{W}(t)$ is a normally distributed random noise satisfying $<\mathbf{W}>=0$ ($<>$ denotes a mean), ζ is the fluid friction force coefficient, D is the diffusion coefficient and $\mathbf{x}$ is the particle position. The velocity is applied to the equation depending on the position the particle occupies at any particular time in the domain. The corresponding probability density function $\mathrm{PDF}(\mathbf{x},t)$ as solved from the Fokker–Planck equation is given by $\mathrm{PDF}(\mathbf{x},\ t) = \frac{1}{\sqrt{4\pi Dt}}\exp(-\frac{(\mathbf{x}-\mathbf{v}t)^2}{4Dt})$. The first and second moments of the particle position are $M_1(\mathbf{x}) = \int_{-\infty}^{\infty}\mathbf{x}\mathrm{PDF}(\mathbf{x},\ t) = <\mathbf{v}t>$ and $M_2(\mathbf{x}) = \int_{-\infty}^{\infty}x^2\mathrm{PDF}(\mathbf{x},\ t) = <v^2t^2> + 4Dt$ (ref. [53]). The second moment equals the MSD of the particle positions. The above relation subtly implies that the MSD is no longer a linear function of time. The diffusion coefficient magnitude in the second moment is replaced using the fluctuation-dissipation theorem, which states the classical Stokes–Einstein formulae as $D_\mathrm{B} = \frac{k_\mathrm{B}T}{6\pi\mu a_\mathrm{p}}$ (where k_B, T, μ and a_p are the Boltzmann constant, absolute temperature, medium viscosity and particle radius, respectively). Using the M_2 relation, we find the evolution of the particle position with time. From these particle trajectories, we employ the MSD analysis to obtain the effective diffusion coefficient for each bacterial layer ($z=z_{1,2,\ldots}$). The diffusion coefficient is plotted normalized by the pure Brownian diffusion (D_B) to get a measure of the enhancement in diffusion due to bacterial colony growth, corresponding to the bacterial layers, $(D/D_\mathrm{B})_{z_{1,2,\ldots}}$. Besides the normalized diffusion coefficient, we also plotted the change in the mean particle position (MSD) and the velocity correlation (Supplementary Fig. 14) to quantify the nature of the transport phenomena.

Reporting summary. Further information on research design is available in the Nature Research Reporting Summary linked to this Article.

Data availability

Data that support the plots within this paper and other findings of this study are available from the corresponding author upon reasonable request. Source data are provided with this paper.

Code availability

All software description, open-source packages and commercial packages are available in the text. All codes that support the analyses and data generation of this study are available from the corresponding author upon reasonable request.

References

47. Shehata, T. E. & Marr, A. G. Effect of temperature on the size of *Escherichia coli* cells. *J. Bacteriol.* **124**, 857–862 (1975).
48. Trueba, F. J., van Spronsen, E. A., Traas, J. & L., W. C. Effects of temperature on the size and shape of *Escherichia coli* cells. *Arch. Microbiol.* **131**, 235–240 (1982).
49. Kumar, P. & Libchaber, A. Pressure and temperature dependence of growth and morphology of *Escherichia coli*: experiments and stochastic model. *Biophys. J.* **105**, 783–793 (2013).
50. Noll, P., Lilge, L., Hausmann, R. & Henkel, M. Modeling and exploiting microbial temperature response. *Processes* **8**, 121 (2020).
51. Berg, S. et al. ilastik: interactive machine learning for (bio)image analysis. *Nat. Methods* **16**, 1226–1232 (2019).
52. Thielicke, W. & Stamhuis, E. J. PIVlab-towards user-friendly, affordable and accurate digital particle image velocimetry in MATLAB. *J. Open Res. Softw.* **2**, 30 (2014).
53. Medved, A., Davis, R. & Vasquez, P. A. Understanding fluid dynamics from Langevin and Fokker-Planck equations. *Fluids* **5**, 40 (2020).

Acknowledgements

This work was supported by the Luxembourg National Research Fund, under the PRIDE Doctoral Training Unit (project MICROH: PRIDE17/11823097), an AFR-Grant (grant no. 13563560) and an ATTRACT Investigator Grant (grant no. A17/MS/11572821/MBRACE to A.S.). This work received generous support from the Human Frontier Science Program Cross Disciplinary Fellowship (J.D., LT000368/2019-C) and the ERC-CoG grant HexaTissue, and by Netherlands Organization for Scientific Research (NWO/OCW) to L.G. We thank P. Wilmes for the *E. coli* C600-WT strain and for the lively discussions during the course of the project. Additional thanks go to C. Martin-Gallausiaux and L. Kleine-Borgmann for microbiological assistance and A. Skupin, M. Desai, J. Najafi and C. Wagner for analytical suggestions during the early phases of this work. We thank G. Eshaghi for assistance with the microparticle assays for transport experiments.

Author contributions

A.S. conceptualized the project, coordinated its operation and provided overall direction of progress. A.T. and A.S. carried out the bacterial growth experiments. J.D. and A.S. carried out the microparticle experiments and J.D. the image processing, PIV analysis and molecular transport simulations. J.D. and A.S. interpreted and presented the analysed data. A.G. provided support with PIV analysis and verified cell geometry data through independent quantification. L.G. developed the continuum model with specific inputs from J.D. and A.S. J.D. prepared the experimental plots and figures. L.G. prepared the computational plots. J.D., A.G., L.G. and A.S. wrote the paper.

Competing interests

The authors declare no competing interests.

Additional information

Supplementary information The online version contains supplementary material available at https://doi.org/10.1038/s41567-022-01641-9.

Correspondence and requests for materials should be addressed to Anupam Sengupta.

Peer review information *Nature Physics* thanks the anonymous reviewers for their contribution to the peer review of this work.

Reprints and permissions information is available at www.nature.com/reprints.

Corresponding author(s): Anupam Sengupta
Email: anupam.sengupta@uni.lu

Last updated by author(s): Anupam Sengupta

Reporting Summary

Nature Portfolio wishes to improve the reproducibility of the work that we publish. This form provides structure for consistency and transparency in reporting. For further information on Nature Portfolio policies, see our Editorial Policies and the Editorial Policy Checklist.

Statistics

For all statistical analyses, confirm that the following items are present in the figure legend, table legend, main text, or Methods section.

n/a	Confirmed	
☐	☒	The exact sample size (*n*) for each experimental group/condition, given as a discrete number and unit of measurement
☐	☒	A statement on whether measurements were taken from distinct samples or whether the same sample was measured repeatedly
☐	☒	The statistical test(s) used AND whether they are one- or two-sided *Only common tests should be described solely by name; describe more complex techniques in the Methods section.*
☐	☒	A description of all covariates tested
☐	☒	A description of any assumptions or corrections, such as tests of normality and adjustment for multiple comparisons
☐	☐	A full description of the statistical parameters including central tendency (e.g. means) or other basic estimates (e.g. regression coefficient) AND variation (e.g. standard deviation) or associated estimates of uncertainty (e.g. confidence intervals)
☐	☒	For null hypothesis testing, the test statistic (e.g. *F*, *t*, *r*) with confidence intervals, effect sizes, degrees of freedom and *P* value noted *Give P values as exact values whenever suitable.*
☒	☐	For Bayesian analysis, information on the choice of priors and Markov chain Monte Carlo settings
☐	☒	For hierarchical and complex designs, identification of the appropriate level for tests and full reporting of outcomes
☒	☐	Estimates of effect sizes (e.g. Cohen's *d*, Pearson's *r*), indicating how they were calculated

Our web collection on statistics for biologists contains articles on many of the points above.

Software and code

Policy information about availability of computer code

Data collection	Availability of computer code statement has been added in the main manuscript file
Data analysis	Availability of computer code (for data analyses) statement has been added in the main manuscript file

For manuscripts utilizing custom algorithms or software that are central to the research but not yet described in published literature, software must be made available to editors and reviewers. We strongly encourage code deposition in a community repository (e.g. GitHub). See the Nature Portfolio guidelines for submitting code & software for further information.

Data

Policy information about availability of data

All manuscripts must include a data availability statement. This statement should provide the following information, where applicable:

- Accession codes, unique identifiers, or web links for publicly available datasets
- A description of any restrictions on data availability
- For clinical datasets or third party data, please ensure that the statement adheres to our policy

Data availability statement is included

Field-specific reporting

Please select the one below that is the best fit for your research. If you are not sure, read the appropriate sections before making your selection.

☒ Life sciences ☐ Behavioural & social sciences ☐ Ecological, evolutionary & environmental sciences

For a reference copy of the document with all sections, see nature.com/documents/nr-reporting-summary-flat.pdf

Life sciences study design

All studies must disclose on these points even when the disclosure is negative.

Sample size	The sample size comprised hundreds of bacterial cells and sysnthetic particles; with each experiment repeated 3 times (both biological and technical replicates were used).
Data exclusions	Not relevant
Replication	At least 3 sets of biological and 3 sets of technical replication was carried in this study
Randomization	Not relevant
Blinding	Not relevant

Behavioural & social sciences study design

All studies must disclose on these points even when the disclosure is negative.

Study description	*Briefly describe the study type including whether data are quantitative, qualitative, or mixed-methods (e.g. qualitative cross-sectional, quantitative experimental, mixed-methods case study).*
Research sample	*State the research sample (e.g. Harvard university undergraduates, villagers in rural India) and provide relevant demographic information (e.g. age, sex) and indicate whether the sample is representative. Provide a rationale for the study sample chosen. For studies involving existing datasets, please describe the dataset and source.*
Sampling strategy	*Describe the sampling procedure (e.g. random, snowball, stratified, convenience). Describe the statistical methods that were used to predetermine sample size OR if no sample-size calculation was performed, describe how sample sizes were chosen and provide a rationale for why these sample sizes are sufficient. For qualitative data, please indicate whether data saturation was considered, and what criteria were used to decide that no further sampling was needed.*
Data collection	*Provide details about the data collection procedure, including the instruments or devices used to record the data (e.g. pen and paper, computer, eye tracker, video or audio equipment) whether anyone was present besides the participant(s) and the researcher, and whether the researcher was blind to experimental condition and/or the study hypothesis during data collection.*
Timing	*Indicate the start and stop dates of data collection. If there is a gap between collection periods, state the dates for each sample cohort.*
Data exclusions	*If no data were excluded from the analyses, state so OR if data were excluded, provide the exact number of exclusions and the rationale behind them, indicating whether exclusion criteria were pre-established.*
Non-participation	*State how many participants dropped out/declined participation and the reason(s) given OR provide response rate OR state that no participants dropped out/declined participation.*
Randomization	*If participants were not allocated into experimental groups, state so OR describe how participants were allocated to groups, and if allocation was not random, describe how covariates were controlled.*

Ecological, evolutionary & environmental sciences study design

All studies must disclose on these points even when the disclosure is negative.

Study description	*Briefly describe the study. For quantitative data include treatment factors and interactions, design structure (e.g. factorial, nested, hierarchical), nature and number of experimental units and replicates.*
Research sample	*Describe the research sample (e.g. a group of tagged Passer domesticus, all Stenocereus thurberi within Organ Pipe Cactus National Monument), and provide a rationale for the sample choice. When relevant, describe the organism taxa, source, sex, age range and any manipulations. State what population the sample is meant to represent when applicable. For studies involving existing datasets, describe the data and its source.*

Sampling strategy	*Note the sampling procedure. Describe the statistical methods that were used to predetermine sample size OR if no sample-size calculation was performed, describe how sample sizes were chosen and provide a rationale for why these sample sizes are sufficient.*
Data collection	*Describe the data collection procedure, including who recorded the data and how.*
Timing and spatial scale	*Indicate the start and stop dates of data collection, noting the frequency and periodicity of sampling and providing a rationale for these choices. If there is a gap between collection periods, state the dates for each sample cohort. Specify the spatial scale from which the data are taken*
Data exclusions	*If no data were excluded from the analyses, state so OR if data were excluded, describe the exclusions and the rationale behind them, indicating whether exclusion criteria were pre-established.*
Reproducibility	*Describe the measures taken to verify the reproducibility of experimental findings. For each experiment, note whether any attempts to repeat the experiment failed OR state that all attempts to repeat the experiment were successful.*
Randomization	*Describe how samples/organisms/participants were allocated into groups. If allocation was not random, describe how covariates were controlled. If this is not relevant to your study, explain why.*
Blinding	*Describe the extent of blinding used during data acquisition and analysis. If blinding was not possible, describe why OR explain why blinding was not relevant to your study.*

Did the study involve field work? ☐ Yes ☐ No

Field work, collection and transport

Field conditions	*Describe the study conditions for field work, providing relevant parameters (e.g. temperature, rainfall).*
Location	*State the location of the sampling or experiment, providing relevant parameters (e.g. latitude and longitude, elevation, water depth).*
Access & import/export	*Describe the efforts you have made to access habitats and to collect and import/export your samples in a responsible manner and in compliance with local, national and international laws, noting any permits that were obtained (give the name of the issuing authority, the date of issue, and any identifying information).*
Disturbance	*Describe any disturbance caused by the study and how it was minimized.*

Reporting for specific materials, systems and methods

We require information from authors about some types of materials, experimental systems and methods used in many studies. Here, indicate whether each material, system or method listed is relevant to your study. If you are not sure if a list item applies to your research, read the appropriate section before selecting a response.

Materials & experimental systems

n/a	Involved in the study
☒	☐ Antibodies
☒	☐ Eukaryotic cell lines
☒	☐ Palaeontology and archaeology
☒	☐ Animals and other organisms
☒	☐ Human research participants
☒	☐ Clinical data
☒	☐ Dual use research of concern

Methods

n/a	Involved in the study
☒	☐ ChIP-seq
☒	☐ Flow cytometry
☒	☐ MRI-based neuroimaging

Antibodies

Antibodies used	Not relevant
Validation	Not relevant

Eukaryotic cell lines

Policy information about cell lines

Cell line source(s)	Not relevant
Authentication	Not relevant
Mycoplasma contamination	Not relevant

Commonly misidentified lines (See ICLAC register)	Not relevant

Palaeontology and Archaeology

Specimen provenance	Not relevant
Specimen deposition	Not relevant
Dating methods	Not relevant

☐ Tick this box to confirm that the raw and calibrated dates are available in the paper or in Supplementary Information.

Ethics oversight	Not relevant

Note that full information on the approval of the study protocol must also be provided in the manuscript.

Animals and other organisms

Policy information about studies involving animals; ARRIVE guidelines recommended for reporting animal research

Laboratory animals	Not relevant
Wild animals	Not relevant
Field-collected samples	Not relevant
Ethics oversight	Not relevant

Note that full information on the approval of the study protocol must also be provided in the manuscript.

Human research participants

Policy information about studies involving human research participants

Population characteristics	Not relevant
Recruitment	Not relevant
Ethics oversight	Not relevant

Note that full information on the approval of the study protocol must also be provided in the manuscript.

Clinical data

Policy information about clinical studies

All manuscripts should comply with the ICMJE guidelines for publication of clinical research and a completed CONSORT checklist must be included with all submissions.

Clinical trial registration	Not relevant
Study protocol	Not relevant
Data collection	Not relevant
Outcomes	Not relevant

Dual use research of concern

Policy information about dual use research of concern

Hazards

Could the accidental, deliberate or reckless misuse of agents or technologies generated in the work, or the application of information presented in the manuscript, pose a threat to:

No	Yes	
☒	☐	Public health
☒	☐	National security
☒	☐	Crops and/or livestock
☒	☐	Ecosystems
☒	☐	Any other significant area

Experiments of concern

Does the work involve any of these experiments of concern:

No	Yes	
☒	☐	Demonstrate how to render a vaccine ineffective
☒	☐	Confer resistance to therapeutically useful antibiotics or antiviral agents
☒	☐	Enhance the virulence of a pathogen or render a nonpathogen virulent
☒	☐	Increase transmissibility of a pathogen
☒	☐	Alter the host range of a pathogen
☒	☐	Enable evasion of diagnostic/detection modalities
☒	☐	Enable the weaponization of a biological agent or toxin
☒	☐	Any other potentially harmful combination of experiments and agents

ChIP-seq

Data deposition

☐ Confirm that both raw and final processed data have been deposited in a public database such as GEO.

☐ Confirm that you have deposited or provided access to graph files (e.g. BED files) for the called peaks.

Data access links *May remain private before publication.*	*For "Initial submission" or "Revised version" documents, provide reviewer access links. For your "Final submission" document, provide a link to the deposited data.*
Files in database submission	*Provide a list of all files available in the database submission.*
Genome browser session (e.g. UCSC)	*Provide a link to an anonymized genome browser session for "Initial submission" and "Revised version" documents only, to enable peer review. Write "no longer applicable" for "Final submission" documents.*

Methodology

Replicates	*Describe the experimental replicates, specifying number, type and replicate agreement.*
Sequencing depth	*Describe the sequencing depth for each experiment, providing the total number of reads, uniquely mapped reads, length of reads and whether they were paired- or single-end.*
Antibodies	*Describe the antibodies used for the ChIP-seq experiments; as applicable, provide supplier name, catalog number, clone name, and lot number.*
Peak calling parameters	*Specify the command line program and parameters used for read mapping and peak calling, including the ChIP, control and index files used.*
Data quality	*Describe the methods used to ensure data quality in full detail, including how many peaks are at FDR 5% and above 5-fold enrichment.*
Software	*Describe the software used to collect and analyze the ChIP-seq data. For custom code that has been deposited into a community repository, provide accession details.*

Flow Cytometry

Plots

Confirm that:

☐ The axis labels state the marker and fluorochrome used (e.g. CD4-FITC).

☐ The axis scales are clearly visible. Include numbers along axes only for bottom left plot of group (a 'group' is an analysis of identical markers).

☐ All plots are contour plots with outliers or pseudocolor plots.

☐ A numerical value for number of cells or percentage (with statistics) is provided.

Methodology

Sample preparation	*Describe the sample preparation, detailing the biological source of the cells and any tissue processing steps used.*
Instrument	*Identify the instrument used for data collection, specifying make and model number.*
Software	*Describe the software used to collect and analyze the flow cytometry data. For custom code that has been deposited into a community repository, provide accession details.*
Cell population abundance	*Describe the abundance of the relevant cell populations within post-sort fractions, providing details on the purity of the samples and how it was determined.*
Gating strategy	*Describe the gating strategy used for all relevant experiments, specifying the preliminary FSC/SSC gates of the starting cell population, indicating where boundaries between "positive" and "negative" staining cell populations are defined.*

☐ Tick this box to confirm that a figure exemplifying the gating strategy is provided in the Supplementary Information.

Magnetic resonance imaging

Experimental design

Design type	*Indicate task or resting state; event-related or block design.*
Design specifications	*Specify the number of blocks, trials or experimental units per session and/or subject, and specify the length of each trial or block (if trials are blocked) and interval between trials.*
Behavioral performance measures	*State number and/or type of variables recorded (e.g. correct button press, response time) and what statistics were used to establish that the subjects were performing the task as expected (e.g. mean, range, and/or standard deviation across subjects).*

Acquisition

Imaging type(s)	*Specify: functional, structural, diffusion, perfusion.*
Field strength	*Specify in Tesla*
Sequence & imaging parameters	*Specify the pulse sequence type (gradient echo, spin echo, etc.), imaging type (EPI, spiral, etc.), field of view, matrix size, slice thickness, orientation and TE/TR/flip angle.*
Area of acquisition	*State whether a whole brain scan was used OR define the area of acquisition, describing how the region was determined.*

Diffusion MRI ☐ Used ☐ Not used

Preprocessing

Preprocessing software	*Provide detail on software version and revision number and on specific parameters (model/functions, brain extraction, segmentation, smoothing kernel size, etc.).*
Normalization	*If data were normalized/standardized, describe the approach(es): specify linear or non-linear and define image types used for transformation OR indicate that data were not normalized and explain rationale for lack of normalization.*
Normalization template	*Describe the template used for normalization/transformation, specifying subject space or group standardized space (e.g. original Talairach, MNI305, ICBM152) OR indicate that the data were not normalized.*
Noise and artifact removal	*Describe your procedure(s) for artifact and structured noise removal, specifying motion parameters, tissue signals and physiological signals (heart rate, respiration).*

Volume censoring

Define your software and/or method and criteria for volume censoring, and state the extent of such censoring.

Statistical modeling & inference

Model type and settings

Specify type (mass univariate, multivariate, RSA, predictive, etc.) and describe essential details of the model at the first and second levels (e.g. fixed, random or mixed effects; drift or auto-correlation).

Effect(s) tested

Define precise effect in terms of the task or stimulus conditions instead of psychological concepts and indicate whether ANOVA or factorial designs were used.

Specify type of analysis: ☐ Whole brain ☐ ROI-based ☐ Both

Statistic type for inference
(See Eklund et al. 2016)

Specify voxel-wise or cluster-wise and report all relevant parameters for cluster-wise methods.

Correction

Describe the type of correction and how it is obtained for multiple comparisons (e.g. FWE, FDR, permutation or Monte Carlo).

Models & analysis

n/a	Involved in the study
☐	☐ Functional and/or effective connectivity
☐	☐ Graph analysis
☐	☐ Multivariate modeling or predictive analysis

Functional and/or effective connectivity

Report the measures of dependence used and the model details (e.g. Pearson correlation, partial correlation, mutual information).

Graph analysis

Report the dependent variable and connectivity measure, specifying weighted graph or binarized graph, subject- or group-level, and the global and/or node summaries used (e.g. clustering coefficient, efficiency, etc.).

Multivariate modeling and predictive analysis

Specify independent variables, features extraction and dimension reduction, model, training and evaluation metrics.